Solid Earth
Discussions

Open Access

EGU

Magnetic properties of pseudotachylytes, Jämtland, central Sweden

Hagen Bender[1], Bjarne S.G. Almqvist[2], Amanda Bergman[3], Uwe Ring[1]

[1]Department of Geological Sciences, Stockholm University , 106 91 Stockholm, Sweden
[2]Department of Earth Sciences, Geophysics, Villavägen 16, 752 36 Uppsala, Sweden
5 [3]Ramböll Sverige AB, Box 17009 , Krukmakargatan 21, 104 62 Stockholm, Sweden

Correspondence to: Hagen Bender (hagen.bender@geo.su.se)

1   Abstract

Nappe assembly in the Köli Nappe Complex, Jämtland, Sweden, has been associated with in- and out-of-sequence thrusting.
Kinematic data from shear zones bounding the Köli Nappe Complex are compatible with this model, but direct evidence

10   from fault zones internally subdividing the nappe complex does not exist. We studied a series of pseudotachylyte exposures
in these fault zones for deciphering the role seismic faulting played in the assembly of the Caledonian nappe pile. To
constrain the fault kinematics, microstructural and magnetic fabrics of pseudotachylyte in foliation-parallel fault veins have
been investigated. Because the pseudotachylyte veins are thin, we focused on small (c. 0.2 cm3) samples for measuring the
anisotropy of magnetic susceptibility. The results show inverse proportionality between specimen size and anisotropy of

15   magnetic susceptibility degree, which is most likely an analytical artifact related to instrument sensitivity and small sample
dimensions. This finding implies magnetic anisotropy results acquired from small specimens demand cautious interpretation.
However, analysis of structural and magnetic fabric data indicates that seismic faulting occurred during exhumation into the
upper crust but yield no kinematic in-formation. Structural field data suggest that seismic faulting was postdated by brittle
E–W extensional deformation along steep normal faults. Therefore, it is likely that the pseudotachylytes formed late during

20   out-of-sequence thrusting of the Köli Nappe Complex over the Seve Nappe Complex.

2   Background

Pseudotachylytes are fault rocks that represent quenched frictional melts generated during co-seismic slip (Magloughlin and
Spray, 1992; Sibson, 1975). Pseudotachylytes have been documented in fault zones within the Köli Nappe Complex, central
Sweden (Beckholmen, 1982). Since the discovery of these localities, almost four decades ago, understanding of

25   pseudotachylyte generation has improved fundamentally (Lin, 2008; Rowe and Griffith, 2015). For example,
pseudotachylyte characteristics have been used to infer dynamics of seismic faulting (e.g., Di Toro et al., 2005). A recently
developed approach exploits magnetic properties and anisotropy of magnetic susceptibility of pseudotachylytes for deducing
the focal mechanism of ancient earthquakes (Ferré et al., 2015). Here we adopt this method to better understand the
kinematics of a ductile-to-brittle shear zone in the Köli Nappe Complex. Such information could offer direct evidence for

30 nappe stacking dynamics along this shear zone within the Köli Nappe Complex. These data are crucial for testing top-to-the-ESE, out-of-sequence fault propagation, which is indicated by map-scale nappe geometry (Beckholmen, 1984) and kinematic data collected elsewhere (Bender et al., 2018). Alternatively, the pseudotachylyte data can be compared to kinematic data from post-orogenic extensional faults crosscutting the nappe architecture (Bergman and Sjöström, 1997; Gee et al., 1994).

1.1 Rock magnetism and its application to pseudotachylytes

Frictional melting significantly affects magnetic properties of fault rocks. The magmatic mineral assemblage of pseudotachylytes commonly is distinctly different from that of its host rock (Ferré et al., 2012). Pseudotachylytes can contain magnetite produced during frictional melting (Nakamura et al., 2002). The rapid quenching leads to a remanent magnetization, which is acquired coseismically but sometimes contains post-seismic superimposed magnetizations, and

40 hence impacts interpretation of paleomagnetism (Ferré et al., 2014; Fukuchi, 2003). Anisotropy of magnetic susceptibility of pseudotachylytes may also record information about the viscous flow of the friction melt (Ferré et al., 2015; Scott and Spray, 1999). Comparison of fault plane geometry and orientation with the magnetic fabric and petrofabric has been used to deduce earthquake kinematics and focal mechanism (Ferré et al., 2015).

The magnetic fabric of a rock is defined by its anisotropy of magnetic susceptibility (AMS), which in turn reflects the sum of

45 individual magnetic responses of the rock-forming minerals (Borradaile, 1987). To use magnetic fabrics for inferring flow direction and sense, the carriers of rock magnetism must be known (Cañón-Tapia and Castro, 2004). In general, minerals respond in three fundamental ways to applied magnetic fields: diamagnetic, paramagnetic or ferromagnetic *sensu lato* (Butler, 1998; Tauxe, 2010). Depending on which of these behaviors is dominant in a rock specimen, AMS needs to be interpreted in different ways. Low susceptibility of diamagnetic minerals generally makes them subordinate contributors to

50 the bulk rock AMS (Hirt and Almqvist, 2012, and references therein). Most rock-forming minerals are paramagnetic, for which AMS is foremost controlled by crystallography. AMS in paramagnetically-dominated rocks reflects the crystallographic preferred orientations of these minerals (Hirt and Almqvist, 2012). For ferromagnetic minerals, AMS is mainly controlled by grain shape and orientation distribution, with the exception of hematite (Borradaile and Jackson, 2010). With few exceptions, paramagnetic and ferromagnetic minerals express normal AMS fabrics. In such fabrics, the longest

55 grain dimensions coincide with the maximum principal AMS axes (Tarling and Hrouda, 1993). For these cases the flow direction can be deduced from the magnetic lineation (Ernst and Baragar, 1992).

3 Regional geological context, field and macroscopic appearance of fault veins

In western Jämtland, the Köli Nappe Complex mainly consists of greenschist- to amphibolite-grade, calcareous metavolcanic and metasedimentary rocks exposed in the Tännforsen Synform (Figure 1; Beckholmen, 1984). Mineral and stretching

60 lineations trend E–W to SE–NW. Foliations dip shallowly and their strikes follow the shape of the synform. Several minor

and two major fault zones separate the thrust sheets of the Köli Nappe Complex. The fault zones show ductile to brittle structures that are associated with pseudotachylyte (Beckholmen, 1982). We investigated the structurally highest of these fault zones, the Finntjärnen fault zone (Figure 1). The Köli Nappe Complex and its underlying units are crosscut by the Røragen Detachment and associated brittle, W-dipping normal faults (Bergman and Sjöström, 1997; Figure 1; Gee et al.,

65   1994). At Finntjärnen (63.389350N, 12.480276E), the schistosity of the micaschist host rock dips shallowly to the WNW (host rock schistosity S_{hr} 302/15, Figure 2a). Mineral and stretching lineations carried by biotite and boudinaged amphibole crystals plunge shallowly to the W (host rock lineation L_{hr} 262/08, Figure 2a). Mylonitic shear sense indicators associated with the ductile fabric were not observed. Fault veins commonly occur as foliation-parallel generation veins and crosscutting injection veins (Figure 2a, Figure 3).

70

The fault veins contain both pseudotachylyte and subordinate ultracataclasite. Macroscopically, four different types of fault rock can be distinguished: (1) **fractured fault rock** occurs in mm to cm wide domains between brittlely undeformed host rock and fault veins. It appears very similar to the host rock, features microscopic fractures and <1 mm to 10 mm-wide injection veins; (2) **cataclasite** has the same color as the host rock, but is much finer grained and appears as patches within

75   fault veins; (3) **pseudotachylyte** displays compositional flow-banding and consists of massive, bright gray, amorphous matrix containing <2 mm-sized clasts of host rock fragments and minerals; and (4) **altered pseudotachylyte** is bluish gray and massive, exhibits layer-parallel banding and generally sharp boundaries to unaltered pseudotachylyte (Figure 3). On slabs cut from an oriented sample (for details, see section 4.1), the coseismic slip direction cannot be deduced from fabrics in the fault vein. Deflection of compositional flow banding and asymmetric injection veins indicate top-to-the-E as well as top-

80   to-the-W sense of shear, respectively.
At the outcrop scale, offset schistosity planes and compositional layering in micaschist along brittle W-dipping, N–S striking faults, commonly occurs (Figure 2b). From orientations and slip sense of these faults, P- and T-axes indicating E–W extension were calculated (Figure 2b). These axes are a kinematic solution that give extensional (T) and contractional (P) directions of strain (Fossen, 2010). Calcite-filled veins crosscut the ductile fabric and the fault veins (Figure 3).

85   **4   Sampling, materials and analytical techniques**

4.1   Sample preparation

An oriented sample of a foliation-parallel fault vein with host rock on either side was collected in the field (sample AB15, schistosity S_{AB15} 341/30, mineral lineation L_{AB15} 269/07; Figure 2 and 3). The hand specimen was cut with a diamond saw into 5 to 10-mm-thick slabs parallel to the lineation and perpendicular to the foliation. A thin section was prepared from one

90   of these slabs. The rest of the slabs were cut into lineation-parallel sticks of approximately equal width and height. From these, 116 cube-shaped specimens were cut for magnetic experiments; x-axes of the cubes are parallel L_{hr} and z-axes are

perpendicular to S_{hr}. Due to small spatial distribution of host/fault rock, specimen cubes are unconventionally small (side length 5.3 ± 1.2 mm, volume 0.17 ± 0.13 cm^3; uncertainty levels here and throughout the manuscript are 1σ) compared to standard-size specimens (7 to 11 cm^3) used in paleomagnetism (Table S1). Therefore, shape and size of cube dimensions

95 were compared to properties of the AMS ellipsoid and uncertainties related to the cube dimension were also investigated. Despite expending particular care in avoiding to cut specimens with different types of host/fault rock, specimens with mixed rock type occur. Approximate modal proportions for each rock type per specimen is presented in Table S2 in the electronic supplementary material.

4.2 Magnetic properties

100 4.2.1 Anisotropy of magnetic susceptibility

Anisotropy of magnetic susceptibility (AMS) was measured using a MFK1-FA susceptibility bridge (Agico, Inc.) operated at 200 A/m alternating current field and 976 Hz frequency. Orientation parameters used for data acquisition with Safyr4W software were P1 = P3 = 6 and P2 = P4 = 0 so that specimen x-axes plunge parallel to L_{hr} and specimen z-axes point upward perpendicular to S_{hr} ("Safyr4W User Manual," 2011). The AMS is expressed by the orientation and magnitude of the

105 principal axes of susceptibility $k_1 \geq k_2 \geq k_3$. Further parameters describing AMS data include the mean susceptibility $k_m = (k_1 + k_2 + k_3) / 3$, , magnetic foliation $F_m = k_2 / k_3$, magnetic lineation $L_m = k_1 / k_2$ and Jelinek's parameter for the degree of anisotropy P_j (Jelinek, 1981). The shape of the susceptibility ellipsoid is described by $T = (\ln[F_m] - \ln[L_m]) / (\ln[F_m] + \ln[L_m])$. Only at $T = +1$ and $T = -1$ is the AMS ellipsoid oblate and prolate, respectively. For $0 < T < +1$, the AMS ellipsoid is more oblate than prolate; for $0 > T > -1$, it is in contrast more prolate (Jelinek, 1981). Mean

110 susceptibility k_m has been normalized for specimen volume.

For data visualization, specimens containing more than one host/fault rock type were plotted based on their modal composition. The specimens were accounted to the dominant host/fault rock type composing the specimen. One specimen containing three rock types and 12 specimens composed of two rock types with each 50% mode were considered as mixed analyses. These data are therefore only presented in the data tables but were excluded from orientation and parameter

115 analysis of AMS data.

4.2.2 Frequency dependence of susceptibility

Frequency-dependent magnetic susceptibility was measured using a MFK1-FA susceptibility bridge (Agico, Inc.) operated at 200 A/m AC field and frequencies of $F_1 = 976$ Hz, $F_2 = 3904$ Hz, $F_3 = 15\,616$ Hz. In order to minimize the effect of anisotropy, all measurements were performed with the sample cubes oriented in the same position with their positive x-axes

120 horizontally pointing toward the operator (POS. 1 in "Safyr4W User Manual," 2011). Frequency dependence of susceptibility is characterized by the parameter $X_{FD} = 100(X_{LF} - X_{HF}) / X_{LF}$ (%) (Dearing et al., 1996).

Solid Earth

Discussions

Open Access

EGU

Frequency dependence is used to identify superparamagnetic magnetite (grain sizes typically <20 nm), as this phase generally shows variation in bulk susceptibility as a function of field frequency. The method was here used to answer the question if very fine-grained magnetite formed during partial melting and recrystallization associated with the fault-slip that 125 formed the pseudotachylyte.

4.2.3 Temperature dependence of susceptibility

Temperature dependence of magnetic susceptibility was measured using a MFK1-FA, equipped with a CS4 furnace. Six sample cubes were analyzed individually; two sample cubes were analyzed together (AB15-13 and AB15-61) because of their small volumes. The samples were ground to a powder with an agate mortar, being careful not to contaminate the sample 130 with outside iron particles or magnetic phases from other materials. Magnetic susceptibility measurements at 200 A/m AC field and 976 Hz frequency were conducted from room temperature up to 700°C, and subsequently cooled back to room temperature, with a heating/cooling rate of 11.8 °C/min. Specimen AB15-67 was measured in air; all other specimens in argon atmosphere. Thermomagnetic data of the empty furnace were smoothed (5-point running mean) and subtracted from the sample thermomagnetic data using the Cureval8 software (Agico, Inc.).

135 4.2.4 Hysteresis

Hysteresis loops were performed with a LakeShore vibrating sample magnetometer with a maximum applied field of 1 T. Data processing was performed with the MATLAB toolbox HystLab (Paterson et al., 2018), using a linear high-field slope correction and automatic drift correction. The hysteresis data was normalized by the mass of the specimen. The extracted hysteresis parameters included saturation magnetization (M_s), saturation remanent magnetization (M_{rs}) and coercivity (H_c).

140 4.3 Shear sense determination using AMS

Obliquity between shear plane and magnetic fabric may be used to determine the sense of slip. Progressive shearing rotates maximum and intermediate principal axes of strain and AMS toward the shear plane (Borradaile and Henry, 1997). Kinematics are indicated in a plane perpendicular to the shear plane (i.e., fault vein margins) that contains the minimum and maximum AMS axes (cf. Figure 26 in Borradaile and Henry, 1997; and Figure 3 in Ferré et al., 2015). In this case, magnetic 145 foliations are inclined toward the slip direction, which gives the sense of shear.

5 Microstructural appearance of host and fault rocks

5.1 Host rock microstructure and petrography

Calcareous amphibole–biotite micaschist hosts the fault veins. Porphyroblastic biotite is oriented sub-parallel to the foliation (Figure 4a). Some grains show minor replacement by chlorite. Very fine-grained (<5 μm), euhedral Ti-oxides occur in the

Solid Earth
Discussions
Open Access
EGU

150   center of patches where chlorite replaced biotite (Figure 5a). Amphibole is completely chloritized and only preserved as pseudomorphs (Figure 4a); their long axes have acute angles (<45°) to the foliation plane. The major opaque mineral is ilmenite (Figure 4a, Figure 5b). Ilmenite breakdown to Ti-oxide is observed at grain boundaries with biotite (Figure 5b). Boundaries between the brittlely undeformed and fractured host rock or fault or injection veins are sharp (Figure 4b). In the fractured host rock, alteration of biotite is more pronounced.

155 **5.2   Fault rock microstructure and petrography**

Cataclastic fault rock appears bright in thin section and consists of granular lithic and mineral fragments (Figure 4c). It forms bulky to drawn-out patches that grade into compositional flow banding in fault veins mainly composed of pseudotachylyte (Figure 3). Within cataclasite patches, tens to hundreds of µm thin, curved to meandering pseudotachylyte veins occur (Figure 4c). The modal abundance of cataclasite patches decreases from bottom to top of the studied fault vein (Figure 3).

160   Only fault rock with microstructural evidence for frictional melting is considered as pseudotachylyte. Such structural evidence includes microcrystallites, sulfide/oxide droplets and spaced survivor clasts, which may display embayed edges witnessing their partial melting (Magloughlin and Spray, 1992; Kirkpatrick and Rowe, 2013). All of these features are expressed in the studied pseudotachylytes. Sulfide/oxide droplets are submicron in size (Figure 4d). Grain size of survivor clasts is on the order of 20 µm to 100 µm (Figure 4d, Figure 5c–d). Their shapes are generally round although some exhibit

165   concave, serrated edges (Figure 5d). Quartz clasts are most common, although microcrystalline subhedral calcite partly appears radial around quartz clasts (Figure 4c). Furthermore, <5-µm-long needle-shaped crystals without obvious shape-preferred orientation occur dispersed in cryptocrystalline or amorphous matrix (Figure 5d). The needle-shaped microcrystallites are probably biotite, as energy-dispersive spectroscopic X-ray (EDS) mapping indicates they are enriched in Al, K, Fe and Mg as compared to the matrix. However, their small size prevented an interpretable single-crystal spectrum.

170   In some places, microcrystallites of unknown composition show dendritic patterns (Figure 5e).

A 4 to 10-mm-wide layer in the upper part of the studied fault vein exhibits a bubbly microstructure in transmitted light (Figure 4e–f). This spherically meandering microstructure represents chlorite alteration fronts replacing pristine pseudotachylyte (Figure 5e). The fine-grained (5 to 15 µm) chlorite displays no shape-preferred orientation. Where chlorite has replaced pseudotachylyte, micron- to submicron-sized, rhomb-shaped Ti-oxide crystals are finely dispersed (Figure 5f–

175   g). Their grain size decreases from center to rim of the chloritized domains.

Thin (<0.5 mm) antitaxial calcite + quartz veins with sharp edges cut across the host rock and all types of fault rock. They consist of mainly calcite and subordinate quartz. Euhedral pyrite occurs within such veins or in close proximity (<1 mm, Figure 3c). Vein orientations generally dip at high angles toward the W or are perpendicular to the foliation. Fibrous calcite, quartz and strain fringes around pyrite are compatible with E–W extension. The veins transect the boundaries between

180   different fault rock types and the host rock without being offset at these boundaries.

6 Rock magnetism results

6.1 Anisotropy of magnetic susceptibility

AMS data for all specimens are summarized in Table 1 and graphically presented in Figure 6. Magnetic anisotropy in host
rock and fault rock specimens displays consistent orientations of principal axes. Maximum principal axes (k_1) trend E–W and
are subparallel the host rock lineation for all rock types (Figure 6). Generally, all rock types show prolate AMS symmetry as
indicated by distribution of intermediate (k_2) and minimum principal axes (k_3) in a girdle perpendicular to k_1. Furthermore,
shapes and orientations of the 95% confidence regions for mean k_2 and k_3 axes reflect the prolate AMS shape (Figure 6a, c–
f). Symmetry of these confidence regions indicates homogeneous AMS fabrics for the analyzed specimen groups (Borradaile
and Jackson, 2010). However, intermediate and minimum principal axes for host rock specimens occur in two clusters
(Figure 6a). One cluster has k_3 axes perpendicular to the host rock foliation and k_2 axes lying within the foliation plane
(Figure 6b). The corresponding sub-fabric AMS ellipsoid approaches oblate shape ($T = 0.21 \pm 0.19$). The magnetic foliation
expressed by these specimens is subparallel to the schistosity S_{hr}. In the second cluster, k_2 and k_3 axes are inversely oriented.
Measurements of anisotropy (P_j, T) scatter over similar ranges for all rock types (Figure 7a). The anisotropy degree P_j shows
highest variation for host rock specimens ($1.02 < P_j < 1.45$); lowest for altered pseudotachylyte ($1.06 < P_j < 1.25$). However,
the median P_j values are similar in all rock types ($1.1 < P_j < 1.2$) and the middle 50% of these data overlap, when shown in
box-and-whisker plots (Figure 7b). The symmetry of the magnetic fabric shows no co-variation with the degree of anisotropy
(Figure 7a). Shapes of AMS ellipsoids for individual specimens of all rock types range from oblate to prolate (Figure 7c).
Overall, neither degree nor shape of the AMS ellipsoid define a magnetic fabric distinctive for one rock type or a group of
several rock types. Nevertheless, the volume-normalized mean susceptibility of altered pseudotachylyte specimens is
approximately twice as high (median $k_m = 4.7 \times 10^{-3}$ [SI]) as that of all other rock types (median $k_m = 2.7 \times 10^{-3}$ [SI]; Figure
8).

6.2 Temperature dependence of magnetic susceptibility

Thermomagnetic curves for heating and cooling of host rock, as well as for pristine and altered pseudotachylyte are
presented in Figure 9a–c. With increasing temperature, host rock thermomagnetic data exhibit steadily decreasing magnetic
susceptibility, followed first by a rapid increase to about twice the initial value at c. 500 °C, and then followed by a rapid
decrease at c. 580 °C (specimens AB15-115, AB15-116; Figure 9d). During cooling, host rock specimens show a prominent
rise in susceptibility at temperatures <600 °C and a peak at c. 430 °C. Pseudotachylyte specimens (AB15-12, AB15-13/61,
AB15-62) show a small but noticeable drop in susceptibility at 550–590 °C (Figure 9e). During cooling, susceptibility rises
sharply for all pseudotachylyte specimens at temperatures <590 °C (Figure 9b). Altered pseudotachylyte exhibits
progressively decreasing susceptibility with increasing temperature without any significant drop (specimens AB15-43,
AB15-67; Figure 9f). During cooling, susceptibility progressively increases to a peak at c. 300 °C and then gradually

decreases again. For specimens AB15-43, there is a small sharp increase of susceptibility at 590 °C observed in the cooling curve.

6.3   Hysteresis loops

Magnetic hysteresis measurements show all rock types respond dominantly paramagnetically to applied high magnetic fields (Table 2, Figure 10a, e, i). Hysteresis results for pseudotachylyte-free specimens show either no or very minor ferromagnetic response. They have saturation magnetizations ($M_s = 2.3 \pm 1.3 \times 10^{-4}$ Am^2 kg^{-1}) about one order of magnitude below those specimens containing pseudotachylyte ($M_s = 1.73 \pm 0.6 \times 10^{-3}$ Am^2 kg^{-1}) (Table 2). Furthermore, pseudotachylyte-free specimens have generally very open slope-corrected hysteresis loops, which do not display branches characteristic of ferromagnetic minerals (Figure 10b, j) (cf. Paterson et al., 2018). Slope-corrected hysteresis curves for these specimens accordingly also display atypical shapes, which may result from an artificial correction to the data (Figure 10c, k). Contrastingly, hysteresis loops for pseudotachylyte-bearing specimens show a ferromagnetic contribution in magnetic response. This is expressed weakly in the unprocessed hysteresis loop (Figure 10e), and more clearly after linear high-field slope correction (Figure 10f; although hysteresis loops generally fail to close at high fields). Based on hysteresis parameters, pristine pseudotachylyte-rich specimens have the highest saturation remanent magnetization ($M_{rs} = 3.9 \pm 1.8 \times 10^{-4}$ Am^2 kg$^-$^{1}), compared to host rock ($M_{rs} = 6.6 \pm 7.5 \times 10^{-5}$ Am^2 kg^{-1}) and altered pseudotachylyte specimens ($M_{rs} = 1.2 \pm 0.5 \times 10^{-4}$ Am^2 kg^{-1}). Magnetic hysteresis raw data is available in Table S3 in the electronic supplementary material.

6.4   Specimen size and shape

Specimen cube dimensions deviate moderately from neutral shapes. Their long edges are between 4.1% and 20.9% longer than their short edges. Prolate and oblate shapes are equally common (Figure 11a, Table S1). The shape parameters of specimen dimensions (T_d) and magnetic anisotropy (T) are independent of each other (Figure 11b, Table S1). The degree of anisotropy of specimen shape and magnetic susceptibility show no significant correlation (Figure 11c).

Raw measurements of mean susceptibility (k_m) and anisotropy degree (P_j) are inversely proportional (Figure 12a). Additionally, the standard error of k_m decreases with increasing specimen volume (Figure 12b). Consequently, the AMS data are dependent on specimen size. Small specimen volumes result in larger uncertainties, which in turn causes higher P_j values. This observation is further discussed in section 7.5 which also discusses the limitation of specimen size in studies using AMS.

240 **7   Discussion**

7.1   Source of magnetic susceptibility and its anisotropy

Thermomagnetic heating curves for host rock specimens show decrease in magnetic susceptibility with increasing temperature until 400 °C, which is characteristic of paramagnetic behavior (Figure 9d) (Hunt et al., 1995). Formation of new magnetite at temperatures above 400 °C is indicated by the peak and sudden decrease in magnetic susceptibility at 580 °C,

245   the Curie temperature of magnetite (Hunt et al., 1995). These results, together with magnetic hysteresis data (Table 2, Figure 10), show that the magnetic susceptibility of the host rock micaschist arises from paramagnetic minerals. It follows that the AMS in the host rock is controlled by the crystallographic orientation of the paramagnetic minerals (Borradaile and Jackson, 2010). An AMS sub-fabric in host rock specimens has parallel magnetic and mineral lineations and sub-parallel magnetic and ductile foliations (Figure 6b). Shape-preferred orientation of tabular biotite crystals in the host rock (Figure 4a) implies

250   crystallographic c-axes of biotite are oriented perpendicular to the schistosity. This AMS sub-fabric is therefore inferred to originate from crystallographic preferred orientation of biotite, which in single crystals exhibits k_3 axes subparallel to biotite crystallographic c-axes (Borradaile and Henry, 1997; Martín-Hernández and Hirt, 2003). The mean magnetic susceptibility k_m of host rock specimens ($k_m = 2.62 \pm 0.46 \times 10^{-4}$, SI) is in the range of typical of schists (km = 0.026–3.0 × 10−3 [SI], Hunt et al., 1995). Single-crystal bulk susceptibility of biotite, muscovite and chlorite are on the same order of magnitude

255   around 10^{-4} [SI] (Martín-Hernández and Hirt, 2003). In the absence of magnetite, the host rock AMS most likely arises from these sheet silicates.

Fractured host rock and cataclasite specimens without pseudotachylyte display the same magnetic properties as host rock specimens (Figures 7, 8, Tables 1, 2). This conformity suggests the same paramagnetic source of the AMS with contributions from biotite, white mica and chlorite.

260   Pseudotachylyte thermomagnetic data shows a distinct drop in susceptibility from 550 °C to 590 °C, which indicates presence of magnetite (Figure 9e). Hysteresis results of pseudotachylyte-bearing specimens show mixed paramagnetic and ferromagnetic behavior (Table 2, Figure 10e–g). The AMS of pseudotachylytes thus reflects the sum of paramagnetic and ferromagnetic minerals in these specimens. The narrow range of k_m does not offer the opportunity to isolate sub-sets (Table 1, Figure 8), which is a common approach to separate AMS sub-fabrics caused by paramagnetic and ferromagnetic minerals

265   (Borradaile and Jackson, 2010). The presence of magnetite does not seem to increase k_m to values significantly higher than the (fractured) host rock and/or cataclasite specimens (Figure 8). The ferromagnetic contribution to the pseudotachylyte AMS is consequently small. The pseudotachylyte AMS is therefore likely controlled by crystallographic preferred orientation of its paramagnetic minerals, that is most probably biotite, with a subordinate contribution from the shape preferred orientation of magnetite (cf. section 5.2).

270   In altered pseudotachylyte specimens, successive decrease in magnetic susceptibility without significant drop at 580 °C during heating indicates dominant paramagnetic behavior. This behavior suggests that magnetite present in pristine pseudotachylyte has been altered to an unknown phase in chloritized pseudotachylyte (Figure 9f). Magnetic hysteresis results

confirm bulk paramagnetic behavior for altered pseudotachylyte (Table 2, Figure 10i–k). The mean magnetic susceptibility for altered pseudotachylyte being about twice as high as that for other rock types (Table 1, Figure 8b), the AMS of altered pseudotachylyte apparently has an additional or a different mineral source than the other rock types. Bulk magnetic susceptibility for single-crystal chlorite without high-susceptibility mineral inclusions is about twice that of biotite and muscovite single crystals (Martín-Hernández and Hirt, 2003). These sheet silicates were also argued to collectively cause AMS in host rock specimens, but in altered pseudotachylyte chlorite is much more abundant, making up to c. 50% of the mode (Figure 4e–f, Figure 5e–g). We infer that AMS in altered pseudotachylyte dominantly reflects the orientation distribution of chlorite.

7.2 Petrofabric versus magnetic fabric orientations

Fault vein margins give the orientation of the slip plane in the Finntjärnen fault zone. Seismic faulting in these veins occurred parallel to the schistosity S_{hr} along subhorizontal, shallowly W-dipping shear planes (Figure 2, Figure 3). The slip direction is indicated by subhorizontal E–W trending magnetic lineation in all fault rock types (Figure 6). This direction is consistent with mineral and stretching lineations expressed in the ductily deformed host rock. These orientations also coincide with the extension direction defined by crosscutting normal faults (Figure 2b). Obliquity between the pseudotachylyte magnetic foliation and fault vein margins would indicate the kinematics of seismic slip (Ferré et al., 2015). However, the AMS of both cataclastic and friction melt-origin fault rocks displays prolate symmetry and magnetic lineations that are parallel with the vein margins. These results show that neither a magnetic foliation nor obliquity with the shear plane are developed, as would be expected from noncoaxial deformation (Borradaile and Henry, 1997). The observed AMS data raises several questions: (1) If such a kinematic model does not agree with the observed fault rock AMS, what process aligned the maximum principal axes? (2) How is it possible to explain the distribution of intermediate and minimum principal axes in a girdle perpendicular to the k_1 axes? (3) Why are AMS fabrics of all rock types compatible? Based on qualitative observations, preferred orientation of pseudotachylyte microcrystallites as well as chlorite in altered pseudotachylyte is absent. Shape-preferred orientation, and thus crystallographic-preferred orientation of the tabular paramagnetic carriers of magnetic susceptibility offers no direct explanation.

7.3 Deformation sequence

Foliation-parallel fault veins, bound by narrow domains of fractured host rock, crosscut the ductile host rock fabric (Figures 2–4). Their formation thus postdated ductile upper-greenschist to amphibolite facies deformation, which is in line with previous work (Beckholmen, 1982; 1983; 1984). Whether chloritization of amphibole occurred before or after fault vein formation is not evident. The fault veins contain unmolten cataclasite, frictional melt-origin pseudotachylyte and altered pseudotachylyte in varying modal amounts. Spaced survivor clasts, microcrystallites and submicron sulfide/oxide droplets in pseudotachylyte identify these fault rocks as quenched, coseismic friction melts (Figure 4, Figure 5) (Magloughlin and Spray, 1992; Cowan, 1999; Rowe and Griffith, 2015). Chloritization of the pseudotachylyte groundmass, and pronounced

305 replacement of biotite to chlorite in fractured host rock domains indicate that hydrothermal alteration was associated with faulting. The chlorite microstructure suggests that recrystallization was static (Figure 5). After pseudotachylyte formation, ambient temperature conditions in the fault zone are therefore inferred to be of lower greenschist-facies (cf. Di Toro and Pennacchioni, 2004; Kirkpatrick et al., 2012). We deduce seismic faulting and subsequent alteration of fault rocks in the Finntjärnen fault zone occurred in the brittle–ductile transition zone near the base of the upper crust. Assuming the typical

310 temperature range of 300–350 °C, and depending on the thermal gradient, the faulting occurred at c. 12 ± 4 km depth (cf. Sibson and Toy, 2006).

Brittle faults and fibrous calcite + quartz veins crosscut both the ductile host rock fabric and the fault veins at high angles. Their orientations relative to the fault vein geometry, together with microscopic and macroscopic observations (Figures 2–5), suggest that these E–W extensional structures formed latest. These structures are consistent with other extensional structures

315 related to the Røragen Detachment west of the Tännforsen Synform (Figure 1) (Gee et al., 1994; Bergman and Sjöström, 1997). In summary, seismic faulting in the Finntjärnen fault zone occurred after the formation of the upper greenschist-/amphibolite-facies schistosity, and prior to late-stage E–W extensional brittle structures. Structural overprinting relations imply transport of thrust sheets in the Köli Nape Complex during exhumation of these nappes from the middle to the upper crust. The sense of faulting can, however, not be deduced from the here presented data. Nevertheless, previous work in the

320 area indicated that thrusting was toward the ESE (Bergman and Sjöström, 1997; Bender et al., 2018).

7.4   Regional tectonic implications

Structural and magnetic analysis of pseudotachylyte-bearing fault veins and their ductily deformed host rocks reveals that petrofabric and AMS are co-parallel. The accordance of these data might indicate that ductile host rock fabrics and brittle fault rock fabrics developed in the same strain field. However, the orientations of AMS and petrofabric in host rock versus

325 fault rock specimens could not be used for deducing the kinematics of neither ductile nor seismic shear. Nevertheless, crosscutting relations show that pseudotachylites formation in the Finntjärnen fault zone predated E–W extensional deformation. Implications on nappe stacking kinematics in the Köli Nappe Complex can nevertheless not be drawn and are left for further investigations. An additional aspect worth clarifying are crosscutting relations in the footwall of the extensional Røragen Detachment in the west of the Tännforsen Synform (Figure 1).

330   7.5   Methodological remarks on AMS of small specimens

There is an apparent inverse relationship between k_m and P_j, as well as a linear relationship between degree of anisotropy and standard error. This effect is caused by specimen size. The larger specimens (by volume) have in general higher bulk susceptibility, and P_j tends towards lower values ranging from 1.01 up to 1.10. Normalization for specimen volume has little impact in removing this bias and it is therefore evident that specimens with very small size are more likely to produce a large

335 scatter in the degree of anisotropy. Although this is an undesired artifact, it demonstrates the limitation of using small sample

cubes in the current setup with the MFK1-FA system. The effect is furthermore emphasized by the increase in k_m standard error as a function of P_j.

Observations of magnetic anisotropy made in this study raises the issue of measuring AMS of specimens with small volume. Current equipment that exists commercially are not designed for handling small specimen volumes and in most applications

340   the intended volume ranges from 7 to 11 cm^3 (representing standard size cubes and cylinders used in paleomagnetic and AMS studies). However, there is a growing interest for measurements of small specimens, as many AMS studies target geological structures that occur on the cm to sub-cm scale (e.g., Ferré et al., 2015). One of the challenges in using smaller specimens is clearly an increased uncertainty in manufacturing specimens that have appropriate dimensions. However, specimens can be constructed with care to compensate for this effect, and in this study, we have demonstrated that the non-

345   equidimensional effect is secondary in importance to the specimen volume. Furthermore, our AMS data show a consistent magnetic fabric in the different rock types, which suggests that they most likely represent the true rock fabric (although the magnitudes are variable).

8   Conclusions

Field, microstructural and magnetic fabric data from the Finntjärnen fault zone provide the following constraints on seismic

350   faulting recorded by pseudotachylyte-bearing fault veins:

(1) Structural overprinting relations show seismic faulting occurred during exhumation of the Köli Nappe Complex into the upper crust within the seismic zone, and before brittle E–W extension.

(2) Neither the petrofabric nor magnetic fabrics reveal the coseismic slip direction.

(3) Chloritization of pseudotachylyte resulted in higher bulk magnetic susceptibility as compared to pristine

355   pseudotachylyte. The very low amount of magnetite in pseudotachylyte, although detectable by its magnetic behavior based on thermomagnetic curves, hysteresis loops and bulk susceptibility, does not contribute substantially to the pseudotachylyte bulk magnetic behavior.

(4) Unconventionally small specimen size increases the degree of anisotropy of magnetic susceptibility measurement data. Magnetic anisotropy results in small specimens demand cautious interpretation, but offers a promising new

360   venue to study detailed geological features.

9   Data availability

All data that led to the conclusions of this paper are presented in the figures, tables and supplementary material.

10   Supplement

Table S1: Mass, dimensions, volume and dimension parameters for individual specimen.

365   Please see separate file 'TableS1SpecimenMassSize.xlsx'

12

Table S2: Approximate proportions of different host and fault rock types for individual specimen.

Please see separate file 'TableS2RockTypeProportions.xlsx'

Table S3: Magnetic hysteresis raw data.

Please see separate file 'TableS3HysteresisRawData.xlsx'

370 **11   Author contribution**

Field work was carried out by HB and AB. HB and BSGA conducted the magnetic experiments, processed and interpreted the results. HB created figures and tables and wrote the initial draft, which was edited by all co-authors.

12   Competing interests

The authors declare that they have no conflict of interest.

375 **13   References**

Beckholmen, M.: Mylonites and pseudotachylites associated with thrusting of the Köli Nappes, Tännforsfältet, central Swedish Caledonides, GFF, 104(1), 23–32, 1982.

Beckholmen, M.: Structural and Metamorphic Zonation in Tännforsfältet Western Jämtland, Swedish Caledonides, Iniv., Stockholm., 1984.

380 Bender, H., Ring, U., Almqvist, B. S. G., Grasemann, B. and Stephens, M. B.: Metamorphic zonation by out-of-sequence thrusting at back-stepping subduction zones: Sequential accretion of the Caledonian internides, central Sweden, Tectonics, doi:10.1029/2018TC005088, 2018.

Bergman, A.: The Pseudotachylites of Tännforsfältet,Western Jämtland, Swedish Caledonides, Stockholm University., 2017.

Bergman, S. and Sjöström, H.: Accretion and lateral extension in an orogenic wedge: Evidence from a segment of the Seve-
385 Köli terrane boundary, central Scandinavian Caledonides, J. Struct. Geol., 19(8), 1073–1091, 1997.

Borradaile, G.: Anisotropy of magnetic susceptibility: rock composition versus strain, Tectonophysics, 138(2–4), 327–329, 1987.

Borradaile, G. J. and Jackson, M.: Structural geology, petrofabrics and magnetic fabrics (AMS, AARM, AIRM), J. Struct. Geol., 32(10), 1519–1551, doi:10.1016/j.jsg.2009.09.006, 2010.

390 Butler, R. F.: Paleomagnetism: Magnetic domains to geologic terranes, Electron. Ed., 23, 1998.

Cañón-Tapia, E. and Castro, J.: AMS measurements on obsidian from the Inyo Domes, CA: a comparison of magnetic and mineral preferred orientation fabrics, J. Volcanol. Geotherm. Res., 134(3), 169–182, 2004.

Ernst, R. E. and Baragar, W. R. A.: Evidence from magnetic fabric for the flow pattern of magma in the Mackenzie giant

radiating dyke swarm, Nature, 356(6369), 511, 1992.

395 Ferré, E. C., Geissman, J. W. and Zechmeister, M. S.: Magnetic properties of fault pseudotachylytes in granites, J. Geophys. Res. Solid Earth, 117(1), 1–25, doi:10.1029/2011JB008762, 2012.

Ferré, E. C., Geissman, J. W., Demory, F., Gattacceca, J., Zechmeister, M. S. and Hill, M. J.: Coseismic magnetization of fault pseudotachylytes: 1. Thermal demagnetization experiments, J. Geophys. Res. Solid Earth, 119(8), 6113–6135, 2014.

Ferré, E. C., Geissman, J. W., Chauvet, A., Vauchez, A. and Zechmeister, M. S.: Focal mechanism of prehistoric

400 earthquakes deduced from pseudotachylyte fabric, Geology, 43(6), 531–534, doi:10.1130/G36587.1, 2015.

Fossen, H.: Structural Geology, Cambridge University Press, Cambridge., 2010.

Fukuchi, T.: Strong ferrimagnetic resonance signal and magnetic susceptibility of the Nojima pseudotachylyte in Japan and their implication for coseismic electromagnetic changes, J. Geophys. Res. Solid Earth, 108(B6), 1–8, doi:10.1029/2002JB002007, 2003.

405 Gee, D. G., Lobkowicz, M. and Singh, S.: Late Caledonian extension in the scandinavian Caledonides-the Røragen Detachment revisited, Tectonophysics, 231(1–3), doi:10.1016/0040-1951(94)90126-0, 1994.

Hirt, A. M. and Almqvist, B. S. G.: Unraveling magnetic fabrics, Int. J. Earth Sci., 101, 613–624, doi:10.1007/s00531-011-0664-0, 2012.

Lin, A.: Fossil Earthquakes: The Formation and Preservation of Pseudotachylytes, Spinger., 2008.

410 Magloughlin, J. F. and Spray, J. G.: Frictional melting processes and products in geological materials: introduction and discussion, Tectonophysics, 204(3–4), 197–204, 1992.

Marrett, R. and Allmendinger, R. W.: Kinematic analysis of fault-slip data, J. Struct. Geol., 12(8), 973–986, doi:10.1016/0191-8141(90)90093-E, 1990.

Nakamura, N., Hirose, T. and Borradaile, G. J.: Laboratory verification of submicron magnetite production in

415 pseudotachylytes: Relevance for paleointensity studies, Earth Planet. Sci. Lett., 201(1), 13–18, doi:10.1016/S0012-821X(02)00704-5, 2002.

Rowe, C. D. and Griffith, W. A.: Do faults preserve a record of seismic slip: A second opinion, J. Struct. Geol., 78, 1–26, doi:10.1016/j.jsg.2015.06.006, 2015.

Scott, R. G. and Spray, J. G.: Magnetic fabric constraints on friction melt flow regimes and ore emplacement direction

420 within the South Range Breccia Belt, Sudbury Impact Structure, Tectonophysics, 307(1–2), 163–189, doi:10.1016/S0040-1951(99)00124-9, 1999.

Sibson, R. H.: Generation of pseudotachylyte by ancient seismic faulting, Geophys. J. Int., 43(3), 775–794, 1975.

Tarling, D. and Hrouda, F.: Magnetic anisotropy of rocks, Springer Science & Business Media., 1993.

Tauxe, L.: Essentials of paleomagnetism, First Edit., University of California Press, Berkeley, Los Angeles, London., 2010.

425 Di Toro, G., Nielsen, S. and Pennacchioni, G.: Earthquake rupture dynamics frozen in exhumed ancient faults., Nature, 436(August), 1009–1012, doi:10.1038/nature03910, 2005.
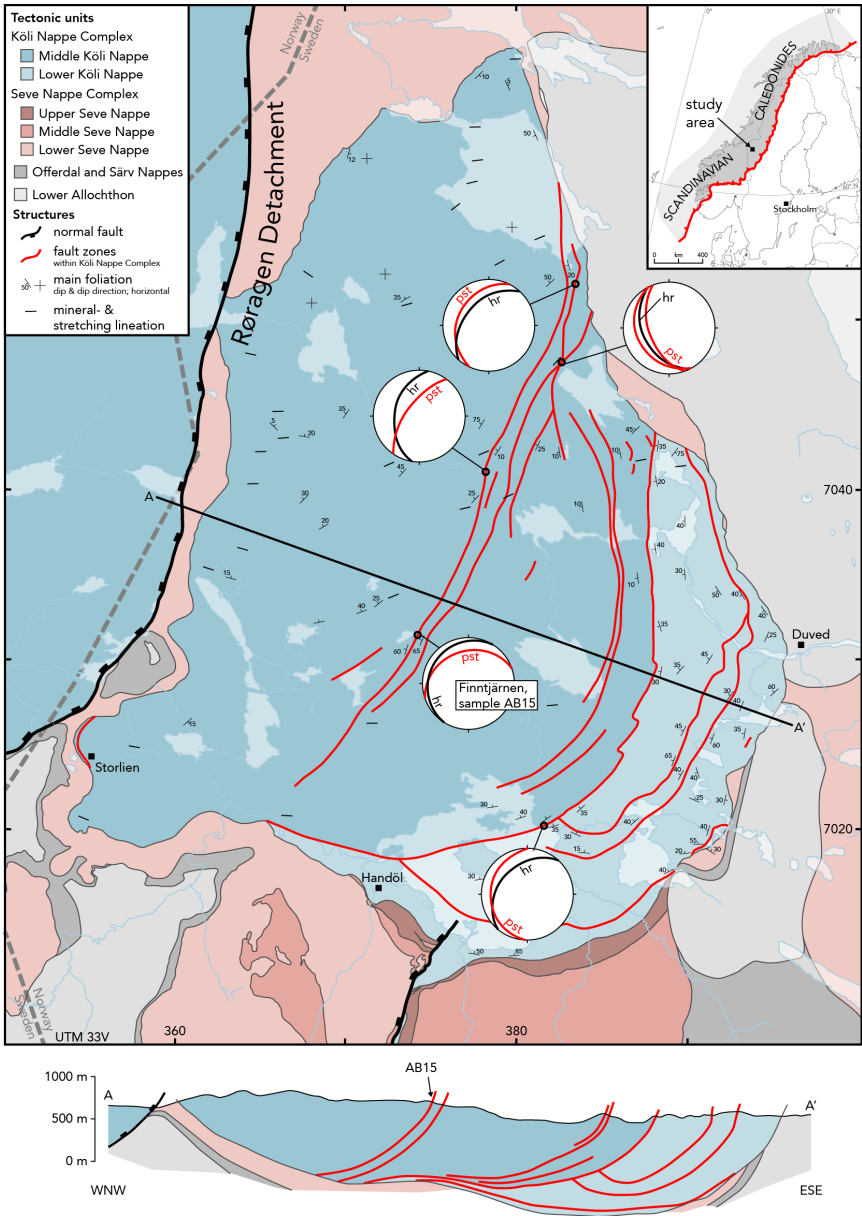
Figure 1. Geological map of the Tännforsen Synform and section A–A′ across it (modified after Beckholmen, 1984). Structural position of tectonic units is indicated in the top left. Structurally lower faults are truncated by structurally higher faults within and beneath the Köli Nappe Complex. Stereographic projections (lower hemisphere, equal-area) show orientations of host rock schistosity (hr) sub-parallel to pseudotachylyte-bearing fault veins (pst) (data from this study and Bergman, 2017). The Røragen Detachment in the west cuts across all other units beneath it, illustrating that it developed structurally latest.

435
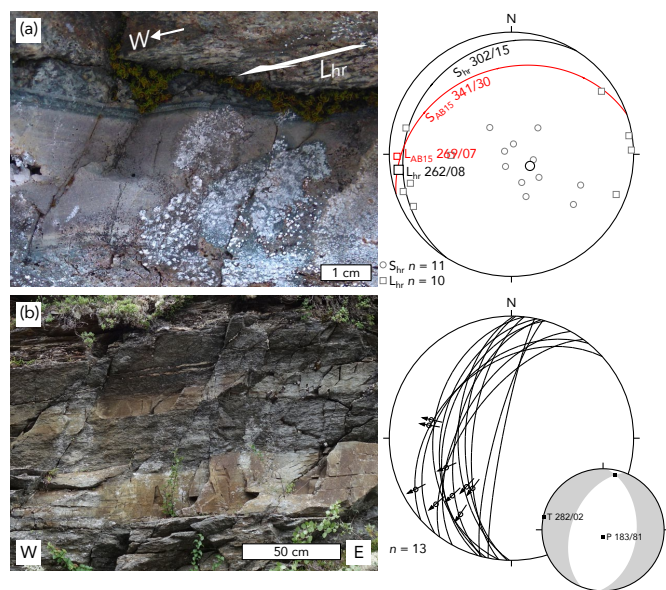
Figure 2. (a) Field photograph of the microstructurally investigated fault vein. It is 3 cm wide, foliation-parallel and exhibits a 5-mm-thick band of bluish, altered pseudotachylyte at its top. Note the crosscutting, steeply dipping fractures. Equal-area projections with poles to host rock schistosity planes (S_{hr}), host rock lineations (L_{hr}) and orientation of the investigated sample AB15 (red great circle). Mean orientations for S_{hr} and L_{hr} are indicated with large symbols. **(b)** Brittle, steeply W-dipping normal faults crosscut the ductile fabric. Sense of slip is indicated by calcite slickenfibres on some of the fault planes. Fault plane solution for these faults (bottom left) shows E–W extension (data processed with FaultKin 7, Marrett and Allmendinger, 1990).
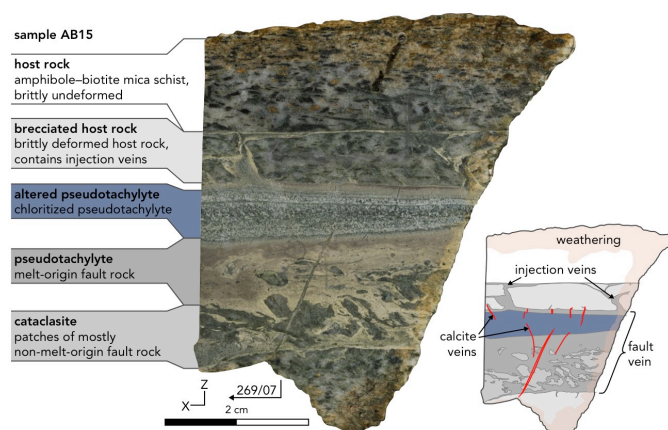
Figure 3. Macroscopic appearance of a foliation-parallel fault vein exhibiting different kinds of fault rock. For detailed description, see text. Characterization of fault rock types is also based on microscopic observations. The image represents the XZ plane of the ductile finite strain ellipsoid.

450
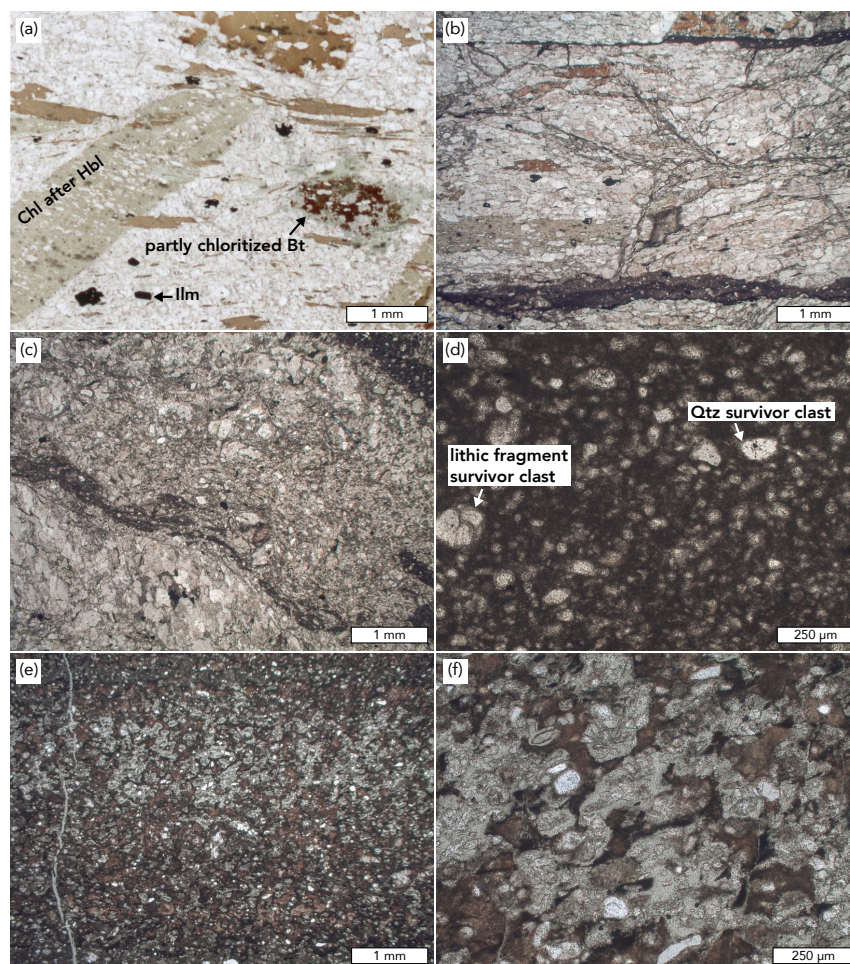
Figure 4. Microstructural appearance of host rock and different fault rock types (plane polarized light). (a) Host rock: foliated micaschist with fine-grained (50–200 µm) quartz + white mica + plagioclase matrix and 1 to 10 mm big porphyroblasts of biotite (fresh: top, partly chloritized: middle right) and pseudomorphs of chlorite after amphibole (left). (b) Brittlely deformed domain in the host rock with multiple fractures filled with cataclasite (center) and/or pseudotachylyte (top and bottom). (c) Cataclastic fault rock: host rock fabric is completely obscured, some lithic fragments remain (bottom left), pseudotachylyte veins occur with patchy and diffuse borders (center, top right corner). (d) Pseudotachylyte: cryptocrystalline matrix containing 20–100-µm-sized, spaced survivor clasts of quartz and lithic fragments. (e–f) Spherulitic appearance of altered pseudotachylyte at different scales.

455

460

19
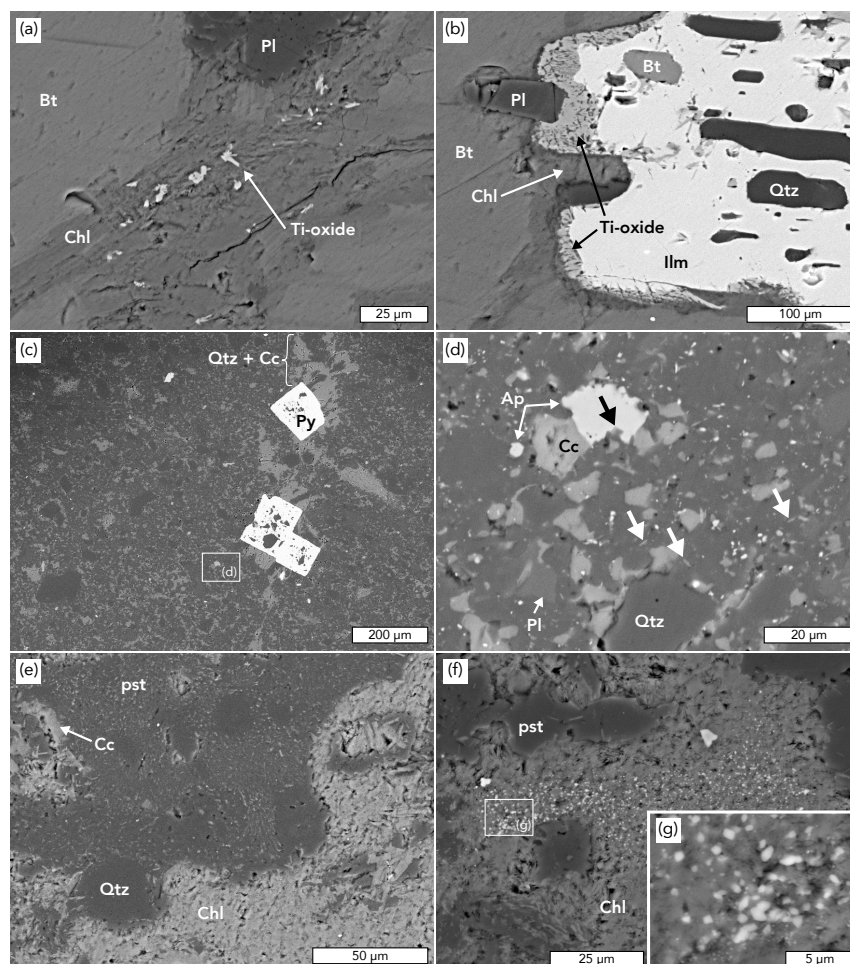
Figure 5. Back-scattered electron images of selected microscopic observations. Mineral abbreviations after Whitney and Evans (2010) (a) Breakdown of biotite to chlorite + Ti-oxide + unidentified K-phase. (b) Reaction rim around ilmenite inclusion in biotite: ilmenite + biotite = Ti-oxide + chlorite + unidentified K-phase. (c) Pseudotachylyte with vertical, crosscutting vein with calcite + quartz + pyrite. (d) Microstructure of pseudotachylyte. Calcite (light gray) and unknown, needle-shaped (white arrows) microcrystallites, and bright, sub-µm-sized oxide/sulfide droplets are dispersed in cryptocrystalline or amorphous matrix. Note embayed edges (black arrow) of an apatite survivor clast versus a much smaller, euhedral apatite crystal further left. (e) Meandering alteration front between chloritized and pristine pseudotachylyte. No preferred orientation of chlorite. Note, in contrast, the fan-like growth of microcrystallites in the matrix. (f-g) Micrometer-sized crystals of Ti-oxide (determined by EDS) finely dispersed in chlorite which replaced cryptocrystalline/amorphous pseudotachylyte (pst).

20
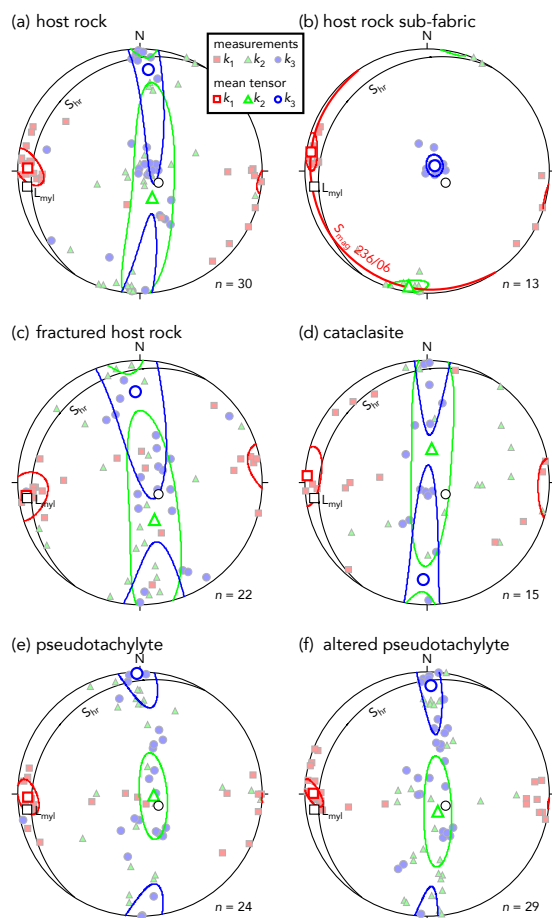
Figure 6. (a–f) Lower-hemisphere, equal-area plots for principal axes of magnetic anisotropy in different rock types. Comments about data presentation: (a) The measurement for specimen AB15-75 was excluded because it was considered as outlier due to its high k_m (cf. Table 1). (e) All data for specimens containing ≥50% pseudotachylyte was plotted. (f) All data for specimens with containing ≥50% altered pseudotachylyte was plotted.

475
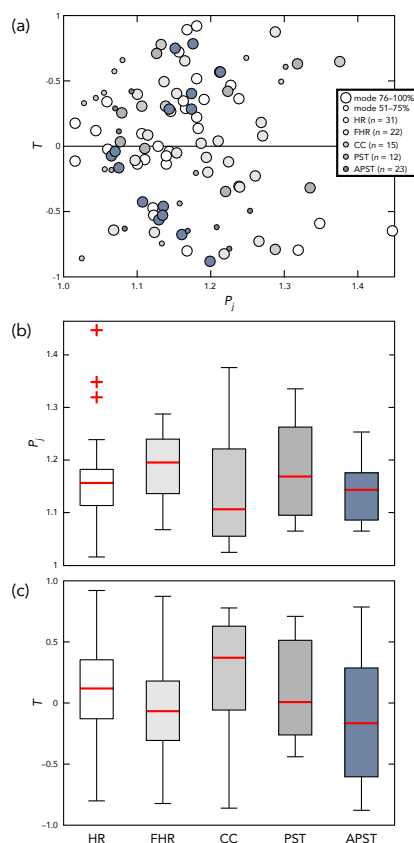
Figure 7. Variation of anisotropy degree (P_j) and shape (T) parameters for AMS of different rock types. None of the rock type is distinct from the others based on these parameters (a). (b–c) Box-and-whisker plots for P_j and T. HR − host rock, FHR − fractured host rock, CC − cataclasite, PST − pseudotachylyte, APST − altered pseudotachylyte.

480
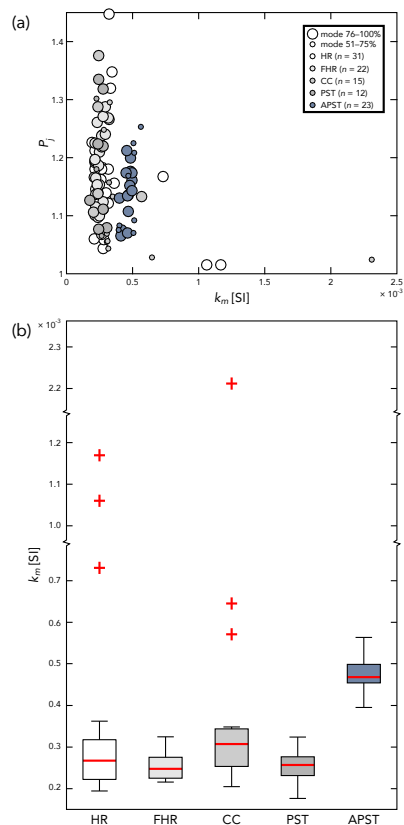
Figure 8. (a) Normalized mean susceptibility (k_m) versus degree of anisotropy (P_j). The mean susceptibility of altered
485 **pseudotachylyte specimens is about twice that of the other rock type specimens (b). For abbreviations, see Figure 7.**
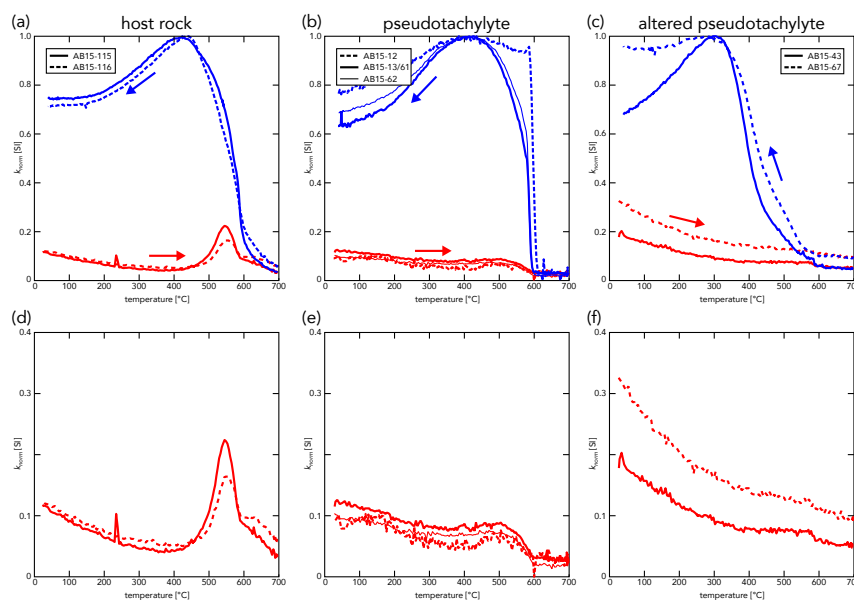
Figure 9. (a–c) Thermomagnetic curves for host rock, pristine and altered pseudotachylyte during heating from room temperature to 700 °C (red curves) and cooling back to room temperature (blue curves). Susceptibility measurements (k_{norm}) were normalized based on the highest value of each sample during the experiment.

490

24
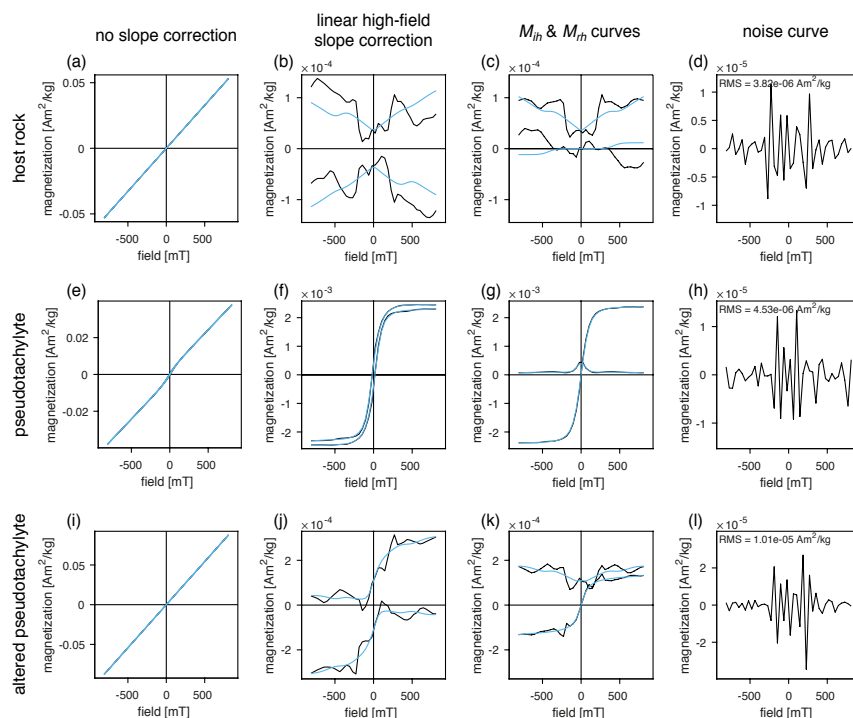
Figure 10. Hysteresis results for selected host rock, pseudotachylyte and altered pseudotachylyte specimens. Dominant paramagnetic behavior of all samples is displayed in raw measurement curves (left column).
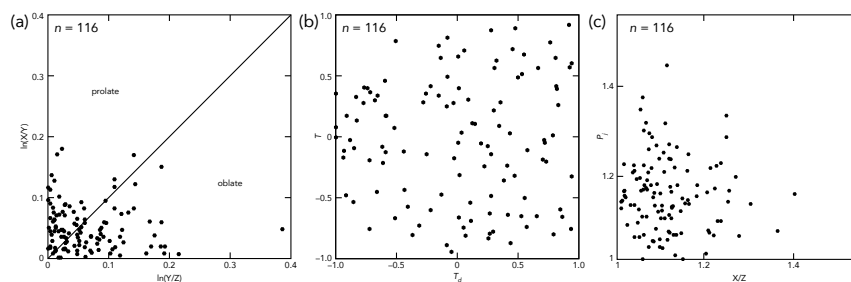
Figure 11. Comparison of shape parameters for specimen cubes and AMS ellipsoids. (a) Flinn diagram of specimen dimensions shows that cubes are not perfectly isometric. (b–c) Specimen shape does not seem to exert an influence on either shape or degree of magnetic anisotropy.

500
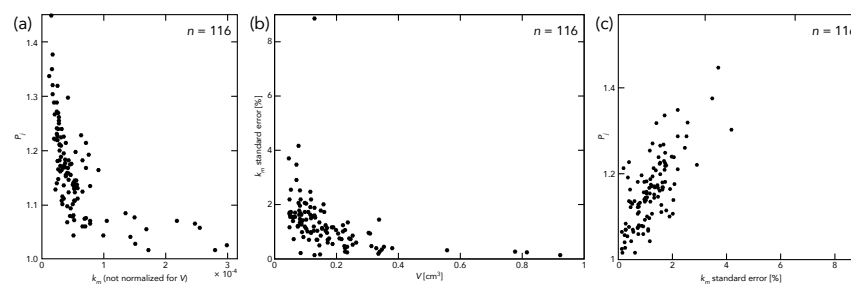
Figure 12. Influence of specimen size on the degree of magnetic anisotropy. (a) Without normalization for specimen volume, anisotropy degree (P_j) decreases with increasing mean susceptibility (k_m). (b) Positive correlation between analytical error and P_j.

505 **Table 1. Anisotropy of magnetic susceptibility data for host rock and different fault rock types.**

| Specimen ID	k_m (raw) $\times 10^{-6}$ [SI]	k_m (norm.) $\times 10^{-6}$ [SI]	std. err. [%]	P_j	T	k_1 declination [°]	k_1 inclination [°]	k_2 declination [°]	k_2 inclination [°]	k_3 declination [°]	k_3 inclination [°]	F test	F12 test	F23 test
Host rock (n = 31). Median k_m = 266 × 10⁻⁶ SI (all data); mean k_m = 332 ± 230 × 10⁻⁶ SI (all data); mean k_m = 262 ± 46 × 10⁻⁶ SI (without outliers)														
mode 76–100%														
AB15-35	17	331	2.5	1.32	-0.79	266	6	358	20	159	69	18.0	29.7	0.3
AB15-36	17	346	2.2	1.35	-0.59	266	3	357	32	172	57	28.5	39.0	1.6
AB15-37	15	324	3.7	1.45	-0.65	265	6	360	36	166	53	15.2	21.8	0.6
AB15-38	35	730	1.6	1.17	-0.80	269	0	359	30	179	60	13.8	21.4	0.2
AB15-72	43	317	0.7	1.12	-0.47	301	16	66	64	205	20	29.5	38.5	4.7
AB15-73	32	271	1.5	1.24	0.36	270	15	100	75	0	3	29.2	7.1	29.3
AB15-74	51	277	1.2	1.04	0.12	223	58	103	17	4	26	1.6	0.9	1.3
AB15-75	172	1169	0.2	1.02	0.11	177	59	17	30	282	9	12.4	8.3	5.7
AB15-76	70	285	0.7	1.06	0.34	131	17	223	5	329	72	8.3	1.7	8.2
AB15-96	51	302	1.0	1.14	-0.13	89	22	257	67	357	4	27.0	21.4	11.5
AB15-97	37	271	1.0	1.18	0.14	90	24	266	66	359	1	37.2	17.3	27.4
AB15-98	43	316	0.7	1.18	0.22	86	24	229	61	349	15	74.9	29.0	59.8
AB15-99	36	245	1.3	1.17	0.89	88	7	236	82	358	4	18.9	0.1	33.1
AB15-100	43	362	0.9	1.16	0.72	91	43	256	46	354	7	32.9	1.1	46.1
AB15-101	29	266	1.7	1.18	0.92	268	7	66	82	178	3	13.2	0.0	23.0
AB15-102	55	234	1.3	1.14	0.04	95	14	286	76	186	3	15.0	10.7	8.1
AB15-103	57	275	0.8	1.11	-0.10	95	11	236	76	4	9	27.9	22.0	13.1
AB15-104	52	240	0.7	1.13	0.00	95	1	197	86	5	4	39.1	25.9	23.1
AB15-105	53	227	0.4	1.12	0.53	89	14	234	73	356	9	101.8	135.7	11.5
AB15-106	43	219	1.1	1.15	0.26	94	8	278	82	184	1	23.7	8.6	22.2
AB15-107	53	242	1.2	1.11	0.10	94	3	284	87	184	0	9.8	5.3	7.1
AB15-108	52	236	1.0	1.14	0.07	88	11	225	75	356	10	24.4	18.3	11.8
AB15-109	50	218	1.1	1.10	-0.13	91	6	243	83	1	3	12.3	10.2	5.4
AB15-110	280	1060	0.6	1.02	0.18	143	14	312	76	52	3	0.7	0.4	0.8
AB15-111	65	212	0.9	1.06	0.02	113	7	22	6	251	81	5.7	3.3	3.2
AB15-112	66	216	1.0	1.18	0.52	108	14	17	3	276	76	42.4	5.8	52.9
AB15-113	71	210	1.5	1.17	0.29	118	13	26	9	263	75	15.5	4.3	14.3
AB15-114	63	193	0.4	1.23	0.46	110	8	19	3	269	82	368.6	62.0	423.9
AB15-115	72	213	0.2	1.21	0.57	111	7	20	4	263	82	1412.3	145.8	1812.5
AB15-116	75	217	0.4	1.19	0.36	108	4	18	7	228	82	342.4	84.7	347.0
AB15-117	92	261	0.4	1.16	0.34	110	7	19	5	257	82	171.3	42.8	171.8

Fractured host rock (n = 22). Median k_m = 247 × 10⁻⁶ SI (all data); mean k_m = 254 ± 32 × 10⁻⁶ SI (all data)

mode 76–100%

AB15-01	27	234	2.5	1.26	-0.23	105	14	15	0	283	76	12.9	12.3	4.1
AB15-02	29	247	2.2	1.21	0.04	85	3	355	5	205	85	11.2	7.1	6.9
AB15-03	36	215	1.3	1.19	0.08	82	0	172	11	350	79	29.5	23.0	13.6
AB15-04	47	247	1.2	1.15	0.05	268	2	177	8	8	82	21.9	16.3	11.4
AB15-05	31	242	1.2	1.19	0.02	251	5	341	7	125	82	28.6	17.8	17.3
AB15-14	35	218	1.7	1.22	-0.12	88	1	178	32	357	58	19.6	15.7	6.6
AB15-15	50	222	0.4	1.14	0.49	86	0	176	23	355	67	138.9	23.4	159.7
AB15-16	54	215	0.9	1.20	-0.20	283	3	192	17	24	73	59.3	54.8	20.0
AB15-34	21	324	1.6	1.27	0.73	265	7	358	19	157	70	34.1	54.4	1.0
AB15-39	26	224	1.9	1.16	0.65	40	23	310	0	220	67	8.2	0.5	11.3
AB15-46	26	265	2.1	1.24	-0.31	76	21	191	47	330	35	14.5	15.3	2.8
AB15-47	24	294	2.0	1.24	-0.31	76	30	196	41	323	34	14.9	16.2	3.1
AB15-54	27	315	1.7	1.27	0.18	80	12	209	72	347	14	28.0	13.5	21.0
AB15-55	24	276	1.3	1.27	0.08	80	20	202	56	340	26	46.9	27.8	25.9
AB15-56	66	274	0.8	1.12	-0.66	78	17	347	4	244	73	33.8	50.9	2.0
AB15-68	38	231	1.0	1.15	0.40	82	37	284	51	180	11	26.1	4.8	27.2
AB15-69	34	224	1.8	1.11	0.09	299	57	60	18	160	27	4.5	2.5	3.0
AB15-70	40	239	1.1	1.10	-0.11	329	66	65	3	156	24	8.1	6.8	3.6
AB15-86	21	269	1.8	1.22	0.82	313	76	56	3	147	14	19.0	29.8	0.2
AB15-87	24	292	2.2	1.29	0.87	271	24	87	66	181	2	18.5	0.1	29.3
AB15-94	41	268	1.1	1.07	-0.64	176	56	311	25	51	21	4.2	5.7	0.2
AB15-95	33	251	1.9	1.10	0.40	178	18	335	71	85	7	3.7	0.8	4.1

Cataclasite ($n = 15$). Median $k_m = 306 \times 10^{-6}$ SI (all data); mean $k_m = 462 \pm 526 \times 10^{-6}$ SI (all data); mean $k_m = 284 \pm 44 \times 10^{-6}$ SI (without outliers)

mode 76–100%

AB15-58	19	238	2.5	1.29	0.79	85	20	191	38	333	46	15.3	23.5	0.2
AB15-59	24	237	2.0	1.14	0.31	326	10	65	40	225	49	4.5	1.4	4.3
AB15-60	32	204	2.0	1.11	0.30	316	2	48	36	224	54	3.0	0.8	2.7
AB15-78	53	570	0.8	1.13	0.78	274	44	86	45	180	4	34.9	0.7	51.2
AB15-79	17	243	3.5	1.38	0.65	270	23	96	67	1	2	11.5	0.8	15.1

mode 51–75%

AB15-10	42	329	8.8	1.30	0.49	127	5	36	11	241	78	1.2	0.1	1.3
AB15-17	299	2312	0.1	1.02	0.86	87	3	185	69	356	21	51.0	83.8	0.4
AB15-18	78	348	0.5	1.13	-0.75	89	7	352	47	185	42	113.2	164.0	2.3
AB15-19	77	306	0.5	1.07	0.57	12	9	105	17	254	71	22.8	2.3	30.3
AB15-20	168	302	0.3	1.05	0.41	79	16	348	3	246	74	38.7	8.2	44.9
AB15-21	99	315	0.5	1.04	0.37	42	5	135	33	305	56	9.6	1.9	9.5
AB15-40	255	313	0.2	1.06	-0.18	86	14	354	7	237	74	75.5	66.3	30.2

AB15-50	151	644	0.2	1.03	0.33	137	37	239	15	346	49	13.4	3.5	14.6
AB15-51	51	288	0.7	1.08	0.66	114	29	232	40	1	36	12.3	0.8	16.5
AB15-77	27	280	1.7	1.25	0.68	266	20	97	70	358	4	22.9	1.2	31.8

Pseudotachylyte ($n = 12$). Median $k_m = 256 \times 10^{-6}$ SI (all data); mean $k_m = 256 \pm 40 \times 10^{-6}$ SI (all data)

mode 76–100%

AB15-12	19	274	2.9	1.22	-0.35	98	6	190	15	346	74	7.1	7.8	1.4
AB15-13	12	241	1.7	1.34	-0.32	82	5	207	82	352	7	43.6	49.6	9.9
AB15-49	45	304	0.9	1.08	0.25	129	29	237	28	2	47	8.5	2.7	7.6
AB15-61	36	276	1.6	1.11	0.02	115	15	16	32	226	54	5.4	3.5	2.7
AB15-62	50	244	0.9	1.08	0.04	99	16	353	44	204	42	8.3	5.0	4.1
AB15-80	25	275	1.4	1.32	0.63	263	43	86	47	354	1	52.3	3.4	67.0
AB15-89	22	175	1.6	1.13	0.71	84	7	334	71	177	18	7.6	0.4	11.3
AB15-90	31	236	1.5	1.22	0.42	89	43	269	47	179	0	24.2	4.0	25.4

mode 51–75%

AB15-09	41	323	1.0	1.16	-0.44	96	9	188	9	323	78	30.5	37.5	4.9
AB15-42	248	268	0.1	1.06	0.18	90	18	355	16	226	66	310.3	275.9	116.8
AB15-82	18	224	4.2	1.30	0.61	261	74	93	15	2	3	5.6	0.6	7.7
AB15-88	26	225	1.6	1.18	-0.21	234	78	346	5	77	11	15.4	14.3	5.1

Altered pseudotachylyte ($n = 23$). Median $k_m = 468 \times 10^{-6}$ SI (all data); mean $k_m = 469 \pm 43 \times 10^{-6}$ SI (all data)

mode 76–100%

AB15-26	29	498	1.5	1.16	-0.68	271	0	1	26	180	64	14.6	21.1	0.6
AB15-27	29	485	1.6	1.20	-0.88	86	0	176	22	356	68	21.2	35.4	0.1
AB15-43	58	402	0.5	1.13	-0.56	105	11	205	42	4	46	80.8	102.5	5.8
AB15-48	55	467	1.0	1.14	0.46	104	11	203	39	0	49	23.8	27.5	2.6
AB15-63	35	464	1.2	1.13	0.53	96	6	199	65	4	25	17.0	22.1	1.6
AB15-64	52	468	0.7	1.11	-0.42	97	12	200	49	357	39	30.2	33.7	3.9
AB15-65	71	415	0.7	1.08	0.17	100	18	9	3	270	71	14.9	12.9	6.3
AB15-66	78	414	0.6	1.06	0.07	83	20	173	2	268	70	18.2	13.9	9.8
AB15-67	105	460	0.3	1.07	0.04	100	22	193	6	298	67	90.3	63.2	51.0
AB15-83	39	478	1.3	1.15	0.75	260	48	92	42	357	6	15.9	0.4	23.1
AB15-84	37	483	2.1	1.18	0.79	262	21	104	67	355	8	8.6	0.2	12.9
AB15-85	38	457	1.3	1.21	0.57	91	12	251	78	0	4	30.8	3.8	41.2
AB15-91	53	497	1.0	1.14	0.28	93	34	260	56	359	6	25.1	7.0	22.9
AB15-92	48	497	1.2	1.17	0.40	93	25	276	65	183	1	25.5	5.4	27.8
AB15-93	46	453	1.5	1.17	0.28	96	33	273	57	5	2	17.0	4.9	15.6

mode 51–75%

AB15-23	38	466	1.6	1.17	-0.65	87	5	183	44	352	45	14.3	19.4	0.6

Solid Earth Discussions — Open Access EGU

AB15-28	31	512	1.4	1.21	-0.62	88	5	181	34	350	55	28.7	38.8	1.4
AB15-29	27	563	1.2	1.25	-0.49	85	1	175	5	341	85	58.8	79.0	7.3
AB15-30	26	506	1.5	1.23	-0.78	88	3	357	29	184	61	27.4	42.1	0.4
AB15-44	136	399	0.3	1.08	-0.63	102	15	194	7	311	74	122.1	175.3	8.5
AB15-45	150	394	0.4	1.08	0.11	83	26	182	17	301	58	45.1	24.9	34.5
AB15-52	46	515	1.0	1.09	0.42	112	9	9	55	208	33	9.2	2.1	9.7
AB15-53	52	507	1.1	1.07	0.29	112	12	2	59	209	28	4.3	1.5	4.0

Mixed specimens with either more than two rock types or 50/50 mode

50% fractured host rock, 25% pseudotachylite, 25% altered pseudotachylite

AB15-71	58	254	0.9	1.06	0.54	52	81	267	8	177	5	6.2	0.7	8.2

50% cataclasite, 50% pristine pseudotachylyte ($n = 6$). Median $k_m = 325 \times 10^{-6}$ SI (all data); mean $k_m = 666 \pm 592 \times 10^{-6}$ SI (all data)

AB15-07	42	278	1.1	1.17	-0.58	103	6	197	36	6	54	26.4	34.5	1.7
AB15-08	56	327	0.6	1.14	0.18	65	3	155	2	273	87	65.1	24.9	51.4
AB15-11	26	323	1.5	1.15	-0.24	73	9	339	24	182	64	12.4	11.1	3.4
AB15-41	218	281	0.3	1.07	0.17	90	15	356	17	219	67	87.9	75.4	33.5
AB15-57	69	1108	0.7	1.07	0.47	80	20	215	62	343	18	13.9	17.1	1.9
AB15-81	142	1680	0.2	1.04	0.82	271	66	89	24	179	1	46.6	0.8	75.6

50% pristine pseudotachylyte, 50% altered pseudotachylyte ($n = 6$). Median $k_m = 448 \times 10^{-6}$ SI (all data); mean $k_m = 427 \pm 57 \times 10^{-6}$ SI (all data)

AB15-22	30	348	1.3	1.17	-0.93	87	4	356	25	185	65	22.0	37.3	0.0
AB15-24	35	460	1.2	1.17	0.72	87	3	179	31	352	59	26.0	38.0	0.7
AB15-25	31	369	1.6	1.16	0.73	88	2	179	33	355	57	13.4	19.6	0.3
AB15-31	25	460	1.7	1.22	-0.77	83	1	352	27	176	63	20.3	31.2	0.4
AB15-32	25	493	1.7	1.23	0.64	84	0	354	28	174	62	22.9	32.3	1.1
AB15-33	29	435	1.7	1.21	-0.74	262	1	352	23	170	67	18.8	29.0	0.5

510 **Table 2. Magnetic hysteresis parameters for processed hysteresis loops (automatic drift correction and linear high-field slope correction, with a cut-off field of 567 mT). Hysteresis data has been mass normalized.**

Specimen ID	mass [mg]	M_s [Am^2/kg]	M_{rs} [Am^2/kg]	B_c [mT]	X [m^3/kg]	Notes
Host rock						
AB15-75	376	1.40E-04	2.06E-05	—	9.22E-08	very open loop
AB15-99	378	4.68E-04	1.78E-04	36.2	8.89E-08	semi-closed loop, closing loop
AB15-115	881	9.41E-05	3.35E-05	—	8.25E-08	very open loop
AB15-116	919	1.01E-04	3.00E-05	—	7.11E-08	very open loop
*Fractured host rock (*5 Vol-% pseudotachylyte)*						
AB15-04	450	3.49E-04	1.92E-04	39.6	8.23E-08	open loop
AB15-16	624	4.01E-04	2.30E-04	50.7	8.10E-08	open loop
AB15-56*	587	1.46E-03	1.51E-04	12.5	9.12E-08	open loop, closing loop
*Cataclasite (and *40 Vol-% or [†]10 Vol-% pristine pseudotachylyte)*						
AB15-17*	315	2.43E-03	3.30E-04	10.4	5.99E-08	open loop
AB15-20*	1419	2.00E-03	2.16E-04	10.8	8.21E-08	open loop
AB15-60[†]	382	1.88E-03	2.37E-04	10.8	7.37E-08	open loop
*Pseudotachylyte (and *20–40 Vol-% or [†]5–10 Vol-% cataclasite)*						
AB15-12	162	1.41E-03	5.50E-04	31.2	5.60E-08	semi-closed loop, closing loop
AB15-13	112	2.01E-03	6.23E-04	28.0	6.30E-08	semi-closed loop, closing loop
AB15-42*	2366	1.10E-03	1.49E-04	11.2	7.54E-08	open loop
AB15-49*	378	1.79E-03	1.95E-04	10.8	7.71E-08	open loop, closing loop
AB15-61[†]	306	2.31E-03	3.00E-04	12.0	7.20E-08	semi-closed loop, closing loop
AB15-62[†]	508	2.38E-03	4.37E-04	17.3	5.51E-08	semi-closed loop, closing loop
AB15-89[†]	282	1.72E-03	4.73E-04	25.4	4.81E-08	open loop
*Altered pseudotachylyte (*and 5 Vol-% pristine pseudotachylyte)*						
AB15-43	337	1.57E-04	1.12E-04	240.0	1.36E-07	very open loop
AB15-48	285	2.17E-04	8.48E-05	—	1.75E-07	very open loop
AB15-67	574	1.35E-04	1.13E-04	54.3	1.75E-07	very open loop
AB15-84*	202	2.40E-04	1.92E-04	108.5	1.82E-07	very open loop
AB15-91	263	2.65E-04	7.83E-05	—	2.00E-07	very open loop